ISSN 1990-7931, Russian Journal of Physical Chemistry B, 2015, Vol. 9, No. 3, pp. 363–374. © Pleiades Publishing, Ltd., 2015.
Original Russian Text © K.A. Avdeev, V.S. Aksenov, A.A. Borisov, R.R. Tukhvatullina, S.M. Frolov, F.S. Frolov, 2015, published in Khimicheskaya Fizika, 2015, Vol. 34, No. 5, pp. 34–46.

COMBUSTION, EXPLOSION, AND SHOCK WAVES

Numerical Simulation of Momentum Transfer from a Shock Wave to a Bubbly Medium

K. A. Avdeev[a, b], V. S. Aksenov[a, b, c], A. A. Borisov[a, b], R. R. Tukhvatullina[b], S. M. Frolov[a, b, c], and F. S. Frolov[a, b]

[a] *Semenov Institute of Chemical Physics, Russian Academy of Sciences, Moscow, Russia*
[b] *Center of Pulse Detonation Combustion, Moscow, Russia*
[c] *National Nuclear Research University "MEPhI", Moscow, Russia*
e-mail: smfrol@chph.ras.ru

Received August 15, 2014

Abstract—Based on the system of equations of two-phase compressible viscous flow, we performed a two-dimensional numerical simulation of momentum transfer by a shock wave propagating from a gas to a continuous aqueous medium or an aqueous medium with air bubbles. When a shock wave impinges on a continuous aqueous medium, the incompressible liquid is set in motion by gas overpressure after the reflection of the shock wave from the gas–liquid interface; however, when a shock wave impinges on a bubbly aqueous medium, the compressible liquid is set in motion due to the penetration of a shock wave into it. Parametric calculations have shown that momentum transfer from a shock wave to a bubbly fluid can be accompanied by dynamic effects, which ensure that the momentum transferred to the bubbly liquid for some time by far exceeds the momentum transferred to a continuous liquid, all other things being equal. These dynamic effects can be used to develop energy-efficient hydrojet propulsion units.

Keywords: bubbly liquid, shock wave, momentum transfer; numerical simulation

DOI: 10.1134/S1990793115030021

1. INTRODUCTION

Most of the modern power plants of water transport vehicles are fitted with bladed propellers, which have a high coefficient of performance (COP), up to 70% [1]. However, with increasing speed of the vehicle, the thrust characteristics of such propellers and their COPs decline; at a speed higher than ~50–60 knots, cavitation arises, which limits the force with which the propeller acts on the outboard water.

For high-speed vehicles, an alternative to bladed propellers is offered by hydrojet propulsion units [2]. In the hydrojet propulsion unit (HPU), the thrust is produced by energy transfer from the heat carrier to the working medium, namely the water in a special flow channel (water duct), with the expanding combustion products of the fuel–air mixture (FAM), high-pressure steam, or the products of reaction of the fuel with water serving as the heat carrier. The main advantage of the HPU is the direct conversion of chemical energy into the kinetic energy of the jet ejected from the water duct.

According to the operation principle, continuous and periodic HPUs are distinguished; the water duct of the continuous HPU operates continuously, whereas that of the periodic HPU operates periodically, with interruptions for preparation of the water for accelerated ejection. In the continuous-flow HPU, as in the air-breathing ramjet engine, the energy input into the working medium occurs at constant pressure, $P = \text{const}$ (Brayton thermodynamic cycle), whereas in pulsed-flow HPUs equipped with valves, the preparation of the water proceeds at constant volume $V = \text{const}$ (Humphrey thermodynamic cycle), during which the pressure of the water in the duct increases, for example due to the combustion of fuel in the adjacent combustion chamber.

Since the thermodynamic efficiency of the Humphrey cycle is higher than that of the Brayton cycle, periodic HPUs must be, in general, more effective than continuous ones. A fuel-fed pulsed-flow HPU can operate in the deflagration (slow) or detonation (fast) combustion modes. It is known that the thermodynamic cycle of detonation combustion (Zel'dovich cycle) provides a higher thermodynamic efficiency of conversion of chemical energy into mechanical work as compared to deflagration combustion at constant volume [3, 4]. Consequently, periodic HPUs with detonation-mode combustion can be quite promising for the water transport.

To make full use of the advantages of the Zel'dovich thermodynamic cycle in periodic HPUs, it is necessary to takes into account the following facts. Because of the large inertia of the water charge in the duct, the detonation wave coming out of the adjacent combus-

tion chamber onto the gas–water interface undergoes multiple reflections before the water begins to rapidly move from the water duct; i.e., all the kinetic energy of detonation products has time to convert into thermal energy. The latter ensures that the combustion in the adjacent combustion chamber actually occurs at constant volume (V = const). In addition, the reflection of the detonation wave from the water surface generates in the water bulk only a weak acoustic wave, imparting practically no momentum to the aqueous medium because of the very low compressibility of water. In this case, the acceleration of the water in the duct begins only after multiple reflections of the detonation wave from the gas–water interface under the influence of the overpressure of the combustion products. However, it is known that the compressibility of the fluid is strongly dependent on the gas content in it: water with gas or vapor bubbles has a much higher compressibility than the continuous water and gas/vapor in the bubbles [5]. For example, the low-frequency speed of sound in water with air bubbles is 40–50 m/s, whereas in water with steam bubbles, only 5–10 m/s, which is significantly less than the speed of sound in water (~1500 m/s) or in air (~340 m/s). Replacement of continuous water by bubbly water enables to take the advantage of detonation combustion noted above: the penetration of a pressure wave of finite amplitude (shock wave) into a bubbly medium would set (without multiple reflections) the bubbly medium as a whole in motion and, hence, would provide a higher momentum of the hydrojet for some period. This idea underlies the patent of invention [6]. Note also that a gas detonation wave interacting with a continuous fluid must inevitably produce gas bubbles. Consequently, in a periodic HPU, bubbly liquid will be present anyway.

The aim of the present work is to develop a computational model of wave propagation in stratified two-phase systems containing continuous and bubbly liquid and to numerically simulate momentum transfer from a shock wave propagating in a gas to continuous and bubbly aqueous media.

2. TWO-PHASE FLOW EQUATIONS

Consider a bubbly liquid composed of two phases, a dispersed gas phase (subscript 1) with a volume fraction α_1 and a dispersion liquid phase (subscript 2) with a volume fraction α_2. Let us introduce the following simplifying assumptions:

(1) during shock compression of a bubbly liquid in a traveling shock wave, the gas does not dissolve in the liquid and liquid does not evaporate into the bubbles;

(2) the shock wave has a relatively low intensity, so that the density of the liquid phase depends only on the fluid temperature T_2;

(3) the flow of the bubbly liquid caused by the shock wave is laminar;

(4) the effects of gravity, buoyancy force, and friction force on the confining surfaces on the relative movement of the phases in the bubbly liquid is negligibly small.

The mathematical model of the interaction of a shock wave with a bubbly liquid is based on two-phase-flow differential equations, derived based on the concept of interpenetrating continua [7], more specifically, the equations of conservation of mass, momentum, and energy of the phases:

$$\begin{aligned}
&\frac{\partial \alpha_1\rho_1}{\partial t} + \nabla \alpha_1\rho_1\mathbf{v}_1 = 0,\\
&\frac{\partial \alpha_2\rho_2}{\partial t} + \nabla \alpha_2\rho_2\mathbf{v}_2 = 0,\\
&\frac{\partial \alpha_1\rho_1\mathbf{v}_1}{\partial t} + \nabla \alpha_1\rho_1\mathbf{v}_1\mathbf{v}_1 = -\alpha_1\nabla p_1 + \nabla \alpha_1\boldsymbol{\tau}_1 + \mathbf{M}_{12},\\
&\frac{\partial \alpha_2\rho_2\mathbf{v}_2}{\partial t} + \nabla \alpha_2\rho_2\mathbf{v}_2\mathbf{v}_2 = -\alpha_2\nabla p_2 + \nabla \alpha_2\boldsymbol{\tau}_2 + \mathbf{M}_{21},\\
&\frac{\partial \alpha_1\rho_1 h_1}{\partial t} + \nabla \alpha_1\rho_1\mathbf{v}_1 h_1 = \nabla \alpha_1\mathbf{q}_1\\
&\quad + \nabla \alpha_1\boldsymbol{\tau}_1\mathbf{v}_1 + \alpha_1\frac{\partial p_1}{\partial t} + H_{12},\\
&\frac{\partial \alpha_2\rho_2 h_2}{\partial t} + \nabla \alpha_2\rho_2\mathbf{v}_2 h_2\\
&= \nabla \alpha_2\mathbf{q}_2 + \nabla \alpha_2\boldsymbol{\tau}_2\mathbf{v}_2 + \alpha_2\frac{\partial p_2}{\partial t} + H_{21}.
\end{aligned} \tag{1}$$

Here, t is the time, ∇ is the differential operator with respect to the coordinates of the radius-vector $\mathbf{r}$, ρ_1 and ρ_2 are the densities of the phases, $\mathbf{v}_1$ and $\mathbf{v}_2$ are the velocities of the phases, p_1 and p_2 are the pressures in the phases, $\boldsymbol{\tau}_1$ and $\boldsymbol{\tau}_2$ are the viscous shear stress tensors for phases 1 and 2, $\mathbf{q}_1$ and $\mathbf{q}_2$ are the heat fluxes in phases 1 and 2, $\mathbf{M}_{12} = -\mathbf{M}_{21}$ and $H_{12} = -H_{21}$ are the terms that describe the interphase transfer of momentum and energy; h_1 and h_2 are the stagnation enthalpies of the phases defined as

$$\begin{aligned}
h_1 &= h_{1,0} + \int_{T_{1,0}}^{T_1} c_{p,1}dT + \frac{1}{2}\mathbf{v}_1\mathbf{v}_1,\\
h_2 &= h_{2,0} + \int_{T_{2,0}}^{T_2} c_{p,2}dT + \frac{1}{2}\mathbf{v}_2\mathbf{v}_2,
\end{aligned} \tag{2}$$

where $c_{p,1}$ and $c_{p,2}$ are the specific heats of the phases at constant pressure, T_1 and T_2 are the temperatures of the phases; the additional subscript 0 denotes to the initial values of the variables.

The system of equations (1) should be supplemented by the following relationships for the fluxes $\boldsymbol{\tau}_1$, $\boldsymbol{\tau}_2$, $\mathbf{q}_1$, $\mathbf{q}_2$, $\mathbf{M}_{12}$, and H_{12}:

$$\boldsymbol{\tau}_1 = \mu_1\left[\left(\nabla\mathbf{v}_1 + \nabla\mathbf{v}_1^T\right) - \frac{2}{3}\nabla\mathbf{v}_1\right],$$

$$\boldsymbol{\tau}_2 = \mu_2\left[\left(\nabla\mathbf{v}_2 + \nabla\mathbf{v}_2^T\right) - \frac{2}{3}\nabla\mathbf{v}_2\right],$$

$$\mathbf{q}_1 = \frac{æ_1}{c_{p,1}}\nabla h_1,$$

$$\mathbf{q}_2 = \frac{æ_2}{c_{p,2}}\nabla h_2,$$

$$\mathbf{M}_{12} = C_D\frac{A\rho_2|\mathbf{v}_{12}|\mathbf{v}_{12}}{8},$$

$$H_{12} = \mathrm{Nu}\frac{æ_2 A(T_1 - T_2)}{d_1},$$

where μ_1 and μ_2 are the dynamic viscosities of phases 1 and 2; $æ_1$ and $æ_2$ are the thermal conductivities of phases 1 and 2; $\mathbf{v}_{12} = \mathbf{v}_1 - \mathbf{v}_2$ is the relative velocity of the phases; d_1 is the diameter of the bubbles; $A = 6\alpha_1/d_1$ is the total area of the interface per unit volume of bubbly liquid; C_D and Nu are the drag coefficient and Nusselt number, which are generally dependent on the Reynolds number of the relative motion of the phases, $\mathrm{Re}_{12} = \rho_2\mathbf{v}_{12}d_1/\mu_2$, and the Prandtl number of the liquid $\mathrm{Pr}_2 = c_{p,2}\mu_2/æ_2$ [7]:

$$C_D = \min\left[\frac{24}{\mathrm{Re}_{12}}(1 + 0.15\mathrm{Re}_{12}^{0.687}),\ \frac{72}{\mathrm{Re}_{12}}\right],$$

$$\mathrm{Nu} = 2 + 0.6\,\mathrm{Re}_{12}^{0.5}\,\mathrm{Pr}_2^{0.33}.$$

The system of eight equations (1)–(2) and the expressions for the fluxes contain 12 dependent variables: α_1, α_2, ρ_1, ρ_2, $\mathbf{v}_1$, $\mathbf{v}_2$, p_1, p_2, h_1, h_2, T_1 and T_2. To close the problem, we used the four additional relations,

$$\rho_2 = \rho_2(T_2),\quad \alpha_2 = 1 - \alpha_1,$$
$$p_1 = \rho_1 R T_1,\quad p_2 = p_1. \tag{3}$$

The system of equations (1)–(3) is supplemented by initial and boundary conditions for the above variables and their derivatives. The last relation in (3), which equates the pressures in the phases, should be treated with some caution. The matter is that, at the identical pressures in the phases, the considered system of equations may lose the property of hyperbolicity. For example, the analysis of system (1) carried out in [8] for an isothermal flow of bubbly liquid at zero fluxes $\boldsymbol{\tau}_1$, $\boldsymbol{\tau}_2$, $\mathbf{q}_1$, $\mathbf{q}_2$, $\mathbf{M}_{12}$ and H_{12} and identical pressures in the phases showed that the matrix of coefficients of the system has complex eigenvalues; i.e., the mixed evolutionary boundary value problem, based on system (1) with zero fluxes is ill-posed: small random perturbations of its solution will grow exponentially over time, with the rate of growth of the perturbation being the higher, the smaller the perturbation wavelength. Taking into account interfacial interactions in system (1) suppresses the instability of the solution; however, upon imposition of a perturbation of greater amplitude, the solution loses stability. To regularize this problem, it was proposed to specify in system (1) different (physically reasonable) pressures in the phases, for example, taking into account the surface tension on the curved interphase interfaces. Similar studies and recommendations on the regularization of problems with multiphase flows are described in [9–11].

Table 1. Geometric dimensions of the shock tubes used in [13–16]

Experimental study	h, mm	L_{HPS}, mm	L_{LPS}, mm	L, mm
[13]	20	1400	160	1850
[14]	40	1150	290	3550
[15]	60	800	200	2000
[16]	30	1500	200	1200

We performed an a priori analysis of the stability of system (1) with nonzero fluxes, which showed that the inclusion of, for example, the momentum fluxes $\boldsymbol{\tau}_1$, $\boldsymbol{\tau}_2$ inside the phases makes the evolutionary problem well-posed (Appendix). To numerically solve system (1), we used a method based on the finite-volume discretization of differential equations with first-order approximation in space and time [12]. To avoid an excessive refining of the computational grid near the solid surfaces with no-slip-flow conditions, the standard method of wall functions was used.

3. TEST CALCULATIONS

To test the predictive capability of mathematical model (1)–(3), we used the experimental results reported in [13–16]. In these works, vertical shock tubes were used to study the characteristics of shock waves propagating from the gas phase to a bubbly water medium (Fig. 1). Shock tubes with a characteristic transverse dimension h consisted of a high-pressure section (HPS) of length L_{D} and a low-pressure section (LPS) of length $L_{\mathrm{LPS}} + L_{\mathrm{TS}}$, separated by a bursting diaphragm (Table 1). The lower part of the LPS was occupied by a column of air-bubbled water of height L_{TS}. After the rupture of the diaphragm at the top of the low-pressure section, filled with air, a shock wave with known characteristics was formed, which then traveled to the bubbly liquid. The velocity of propagation and other characteristics of the shock wave in the bubbly liquid were measured using pressure sensors (DD) mounted in the test section (TS). High-speed

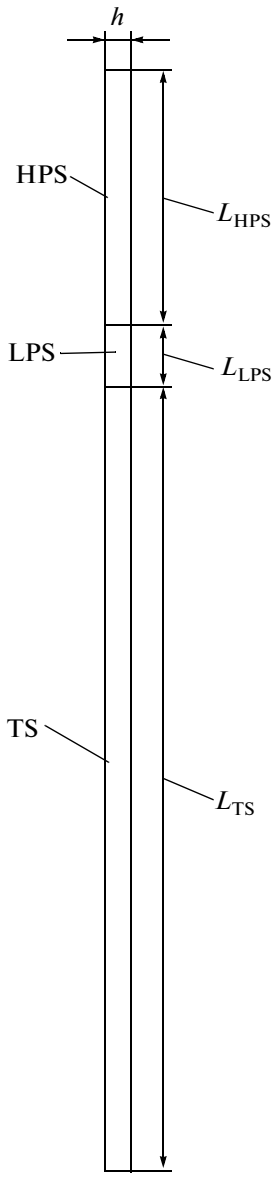

Fig. 1. Schematic diagram of the shock tubes used in [13–16] to study the propagation of shock waves in bubbly liquids.

photography frames were taken through optical windows in the TS.

The computational grid was refined until the result became independent of the computational grid cell size. Further refinement of the computational grid and reduction of the time step did not affect the calculated propagation velocity of the shock wave propagation through the bubbly liquid.

3.1. Experimental Data from [13]

In experiments conducted by the authors of [13], the high-pressure section and low-pressure section were filled with air at room temperature and pressures of 4 and 1 atm, respectively. A water column of height 1850 mm was saturated with air bubbles with an average initial (index 0) diameter of $d_{10} = 2$ mm and an initial volume fraction of gas of α_{10} =0.01 to 0.2. The shock wave velocity in the bubbly liquid D was determined from the records of sensors DD1 and DD2 (Fig. 2a) by dividing the distance between them by the time interval between the arrival of the wave at sensors DD1 and DD2. Figure 2b compares the calculation results (curve) with the experimental data from [13] (symbols), more specifically, the dependence of the shock wave velocity within the measurement segment DD1–DD2 on α_{10}. The calculations were performed in the two-dimensional approximation for the actual basic geometric dimensions of the shock tube used in [13]. The average calculated velocity of the shock wave was determined in the same manner as in the experiment: from the distance between control sections DD1 and DD2 and the time it takes for the wave front to traverse this distance. Figure 2b shows that the calculation and experimental results are in good agreement at $\alpha_{10} > 2$–3%, while at lower values of α_{10}, a large discrepancy is observed. The latter is apparently due to the violation of the assumption of continuity of the dispersed phase (bubbles) under such conditions: bubbles in the water are located far apart, so that the shock wave appears to interact with individual bubbles. Figure 2b also shows that the shock wave velocity in water with air bubbles is 50–150 m/s, which is substantially less than the velocity of sound in water (~1500 m/s) and air (340 m/s).

3.2. Experimental Data from [14]

In experiments performed by the author of [14], a high pressure in the HPS (24 and 36 atm) was obtained by burning an acetylene–oxygen mixture, whereas the LPS was filled with air at atmospheric pressure; the test section was occupied by a 3550-mm-high water column with air bubbles of mean diameter $d_{10} = 2.5$ mm; the initial volume fraction α_{10} of gas phase ranged from 0.005 to 0.06. The air and water were at room temperature. The shock wave velocity in the bubbly liquid was determined from the signals of sensors DD1, DD2, and DD3 (Fig. 3a) by dividing the distance between the sensors by the time interval between the arrival of the wave at sensors DD1 and DD2. Figure 3b compares the calculation results (curve) with the experimental data from [14] (symbols): the shock wave velocity within the measurement distances DD1–DD2 and DD2–DD3 versus α_{10} at two gas pressures (24 and 36 atm) in the HPS. The calculations were performed in the two-dimensional approximation for the actual basic geometrical dimensions of the shock tube [14]. The average calculated velocity of the shock wave was determined in the same manner as in the experiment, by dividing the distance between the control sections DD1–DD2 and DD2–DD3 by the travel time of the wave front over these sections.

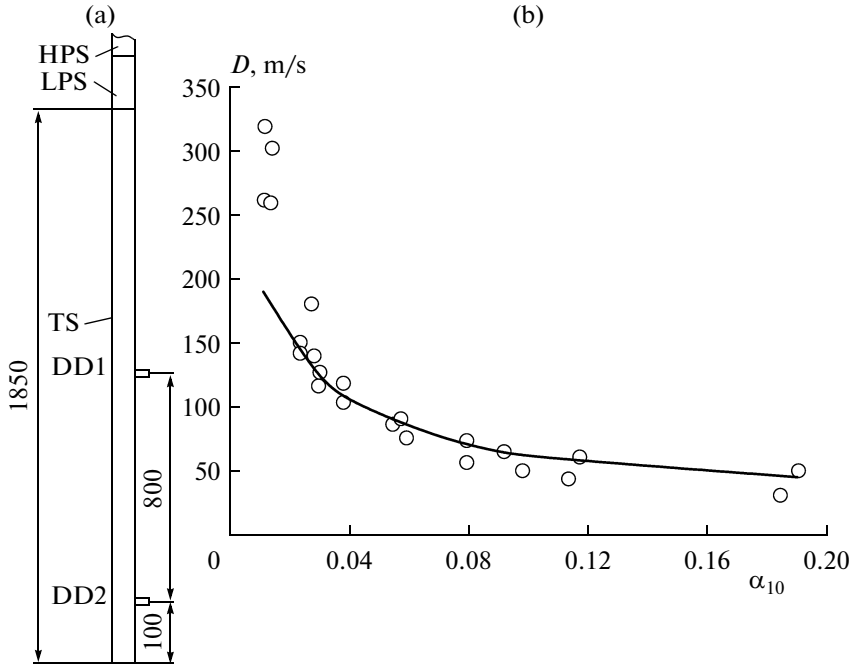

Fig. 2. (a) Schematic diagram of the experimental setup used in [13] (dimensions in mm); (b) comparison of the calculated (curve, present work) and measured (symbols [13]) dependences of the shock wave velocity within measurement segment DD1–DD2 on the volume fraction of air bubbles in the water.

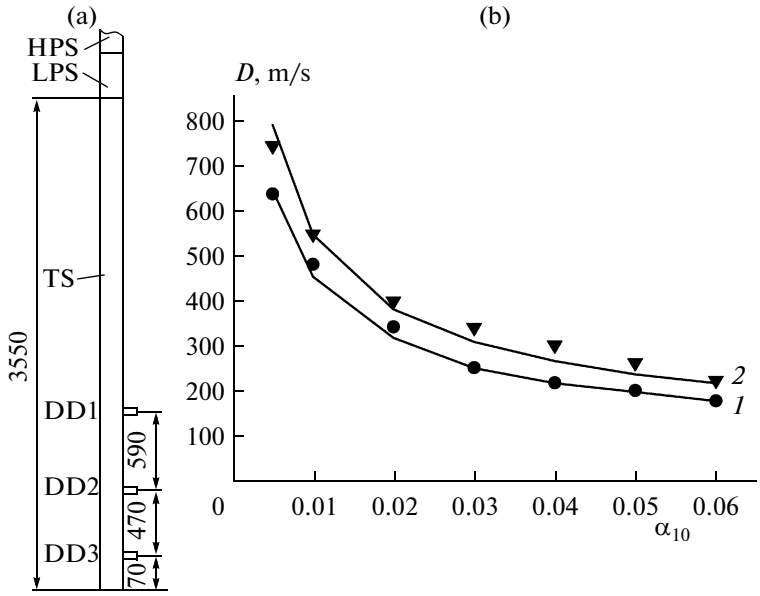

Fig. 3. (a) Schematic of the experimental setup used in [14] (dimensions in mm); (b) comparison of the calculated (curves, present work) and measured (symbols [14]) dependences of the shock-wave velocity within measurement segments DD1–DD2 and DD2–DD3 on the volume fraction α_{10} of air bubbles in the water at different pressures in the HPS: (●, *1*) $p_{HPS} = 24$ atm and (▼, *2*) 36 atm.

Note that, for the given values of α_{10} and pressure in the HPS, the shock wave velocities calculated for the measurement distances DD1–DD2 and DD2–DD3 did not differ from each other. Figure 3b demonstrates that the calculation and experimental results are in good agreement, even at $\alpha_{10} = 0.005$. It should be emphasized that, in the experiments performed in [14], the shock waves in water with air bubbles were considerably stronger than in the experiments carried out in [13]. For example, at the same initial volume fraction of gas phase, $\alpha_{10} = 0.02$ and nearly identical average sizes of the air bubbles, the shock wave velocity

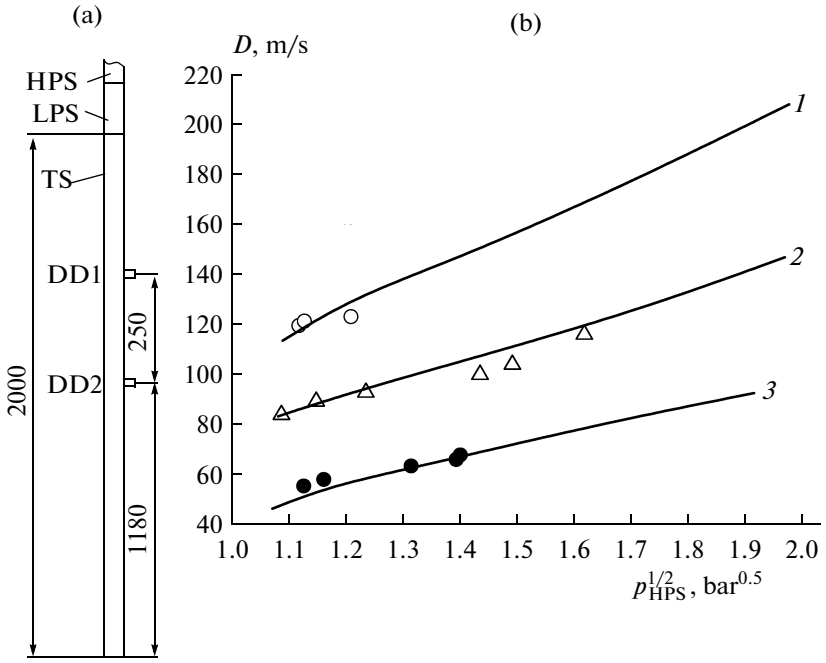

Fig. 4. (a) Schematic diagram of the experimental setup used in [15] (dimensions in mm); (b) comparison of the calculated (curves, present work) and measured (symbols [15]) dependences of the shock-wave velocity within measurement segment DD1–DD2 on the pressure in the HPS p_{HPS} at different initial volume fraction of air bubbles α_{10} in water–glycerol solutions: (○, *1*) 0.01, (△, *2*) 0.02, and (●, *3*) 0.05.

was 150 m/s in [13] and 300 and 400 m/s in [14], whereas at $\alpha_{10} = 0.05$, it was 100 m/s in [13] and 200 and 250 m/s in [14].

3.3. Experimental Data from [15]

In the experiments conducted by the authors of [15], the air pressure in the HPS was varied from 1.2 to 4 atm, while the LPS was filled with air at atmospheric pressure. A 2000-mm-high column of water–glycerol solution (kinematic viscosity 2×10^{-6} m^2/s) containing air bubbles with an average diameter of $d_{10} = 2.0$ mm was placed in the test section of the shock tube; the gas phase volume fraction was $\alpha_{10} = 0.01$, 0.02, and 0.05; the air and solution were at room temperature. The shock wave velocity in the bubbly liquid was determined using the signals from sensors DD1 and DD2 (Fig. 4a) by dividing the distance between the sensors by the time interval between the arrivals of the wave at sensors DD1 and DD2. Figure 4b compares the calculation results with the experimental data in the form of the dependence on the shock-wave velocity measured over the DD1–DD2 distance on the pressure in the HPS. As can be seen from Fig. 4b, the calculation and experimental results are in good agreement at both $\alpha_{10} = 0.01$ and $\alpha_{10} = 0.02$ and 0.05.

Table 2. Main parameters of two runs from [16]

Run no.	d_{10}, mm	α_{10}	P_{HPS}, atm	P_{LPS}, atm
1	3.8	0.027	2.27	2.02
2	5.0	0.0077	1	1

3.4. Experimental Data from [16]

The authors of [16] performed two experiments on the optical detection of the velocity of gas bubbles behind a shock wave propagating in a vertical column of water with air bubbles in the test section of a shock tube. The initial pressure and temperature of the air and water corresponded to normal atmospheric conditions. The basic parameters of the experiments [16] are listed in Table 2.

Figures 5a and 5b compare the calculation results (curves) with the experimental data in the form of the time evolution of the velocity of the bubbles for two experiments from [16]. A satisfactory agreement between measurements and simulations is observed. Note that, in [16], a high-speed cinematography was used to record the velocity of a single air bubble set in motion by the shock wave, while the simulations yielded the velocity of the entire dispersed component of the bubbly liquid, without regard for the deformation of the gas bubbles during their movement.

4. TRANSFER OF MOMENTUM FROM THE SHOCK WAVE TO THE BUBBLY MEDIUM

The above test calculations give reason to believe that the mathematical model of two-phase flow based on system (1) properly describes the dynamics of the interaction of a shock wave with a bubbly medium. This enables to formulate and solve an important problem of momentum transfer from a shock wave to a bubbly medium.

Consider the schematic diagram of a model device displayed in Fig. 6. The device consists of a water duct (a wide straight channel of constant cross section, 850 mm in length and 100 mm in width, with two open ends) and a shock wave generator (a gas channel of width 50 mm with HPS and LPS sections separated by a diaphragm), with one of the channel ends being open, communicating with the water duct. Suppose that the entire device is immersed in a continuous aqueous medium, the HPS is filled with high-temperature high-pressure combustion products, the LPS is filled with air under normal conditions, whereas the parts of the water duct adjacent to it (regions I–III in Fig. 6) can be filled with bubbly water. Differences in the hydrostatic pressure at different points of the computational domain are assumed negligible. Figure 6 specifies all the dimensions of the model device, whereas Table 3 lists all the input parameters of the problem. To curtail the computational cost, the problem of transfer of momentum from the shock wave to the bubbly flow was solved for half the water duct, so that the computational domain was limited from below by a symmetry plane, as shown in Fig. 6. The three other boundaries of the computational domain (left, right, and top) were set far away from the water line, so that they would not influence the flow in the water duct and its immediate neighborhood.

Two series of calculations were performed. In the first series, air bubbles were introduced only in region I inside the water duct, adjacent to the outlet section of the shock wave generator. The initial volume fraction of water in the region I was $\alpha_{20} = 1.0$, 0.97, 0.94, 0.90, and 0.80. In the second series of calculations, air bubbles were introduced into region I of the water duct, regions I and II, or regions I, II, and III, whereas the initial volume fraction of water in the bubbly medium was fixed at 0.90. In all calculations, at the initial time, all the media (gas in the HPS, gas in the LPS, water in the water duct and outside it, as well as the bubbly liquid in the water duct) were at rest. The movement began after the instant opening of the diaphragm that separates the HPS and LPS. As a result, an air shock wave was formed, which after a short time, first penetrated into the bubbly liquid and then propagated into the continuous water in the water duct and outside it, undergoing reflections and diffraction.

Figure 7 shows spatial distributions of the volume fraction of water α_2 in the calculation domain at different instants of time after the opening of the diaphragm in the shock wave generator (after 1, 5, 10, 15, and 20 ms) for a bubbly water charge ($\alpha_{20} = 0.9$, left) and for a continuous water charge ($\alpha_{20} = 1$, right). A comparison of the distributions on the left and right clearly shows differences between them starting from the time 5 ms. When the shock wave emerges from the bubbly water charge, a zone with a high gas content is rapidly formed near the right edge of the water duct wall, which later merges with the gas coming from the shock wave generator. By the time 20 ms, the sizes of the gas bubble at the water duct outlet for the two above cases were significantly different.

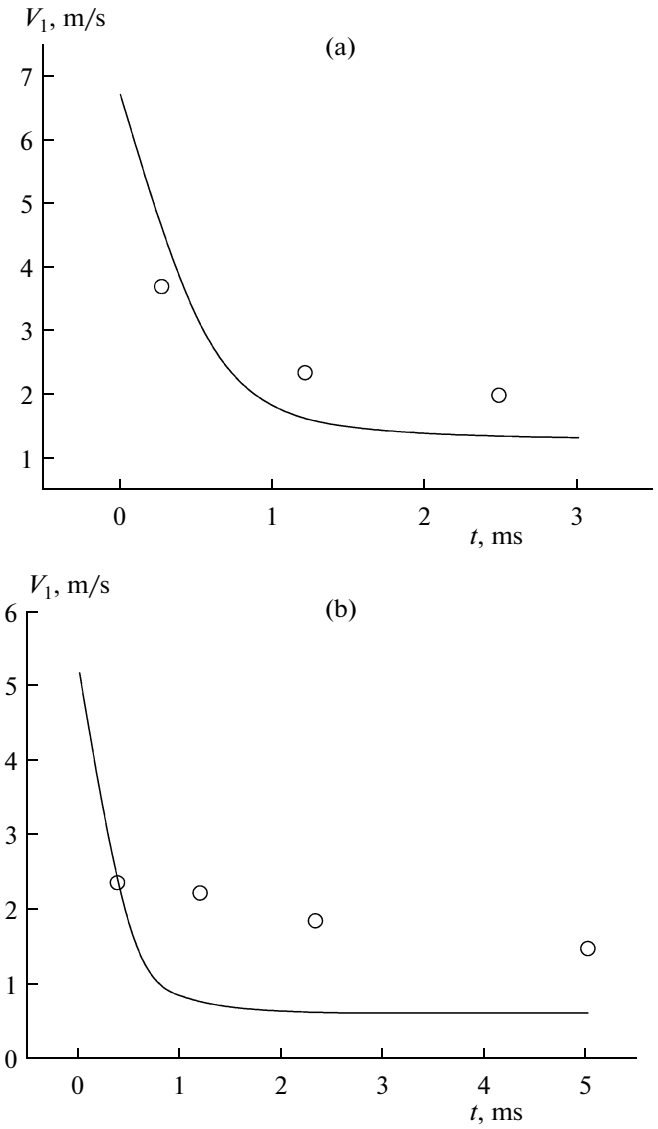

Fig. 5. Comparison of the calculation results (curves, present work) with the experimental data (symbols) [16] on the time evolution of the velocity of a gas bubble set in motion by a shock wave: (a) run 1, (b) run 2 in Table 2.

The instantaneous force acting on the device is given by

$$F(t) = I_{\text{in}}(t) - I_{\text{out}}(t),$$

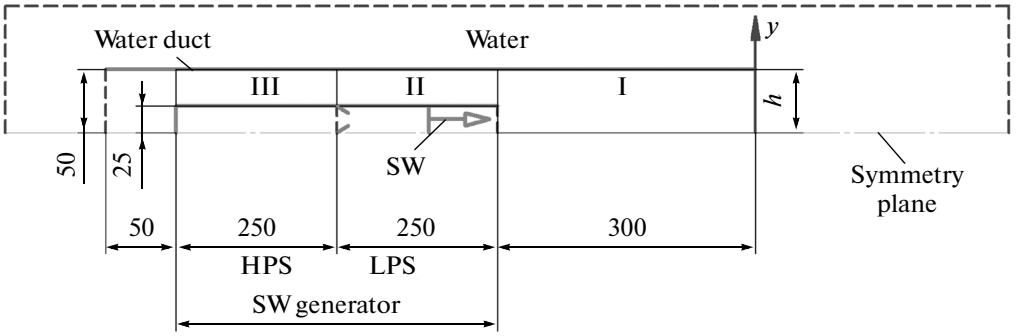

Fig. 6. Schematic diagram of the model device for calculating the momentum transfer from a shock wave to a bubbly medium (dimensions in mm).

where

$$I_{in}(t) = \int_0^h [p_{in}(t,y) + \rho_{in}(t,y)u_{in}^2(t,y)]dy,$$

$$I_{out}(t) = \int_0^h [p_{out}(t,y) + \rho_{out}(t,y)u_{out}^2(t,y)]dy.$$

Here, the indices "in" and "out" correspond to the left and right sections of the water duct of halfwidth h = 50 mm, and y is the transverse coordinate (Figs. 6 and 7). The force F is considered positive if it is directed from the right to the left in Figs. 6 and 7.

Figure 8 shows the time evolution of the instantaneous force F for the two cases specified in Fig. 7 throughout the calculation time (Fig. 8a) and within the initial 20 ms (Fig. 8b). In either case, the entire process of momentum transfer from the shock wave to the liquid (both continuous and bubbly) can be divided into four stages. In the first stage, the action of the shock wave on the fluid in the water duct dominates. In the second stage, the wave-mode action gives way to the piston-mode action of the high-pressure gas on the liquid in the duct. In the third stage, the piston-mode action declines due to the escape of a gas bubble through the right end of the duct. Finally, in the fourth stage, the pressures of the liquid and gas in the duct equilibrate, and momentum transfer stops.

Table 3. Parameters of the problem of momentum transfer from a shock wave to a bubbly liquid

Parameter	Value
L_{LPS}, mm	250
L_{HPS}, mm	250
L_{WD}, mm	850
Pressure in HPS, atm	15.5
Temperature in HPS, atm	3957
Pressure of air in LPS, atm	1
Temperature of air in LPS, atm	293.15
Temperature of water, K	293.15
Volume fraction of gas in the water charge α_{10}	0, 0.03, 0.06, 0.1 and 0.2

As can be seen from Fig. 8, during the first stage, short-term peaks of positive and negative instantaneous forces arise, caused by reflections of the shock wave and rarefaction wave formed in the gas channel, as well as in the stratified medium, and in the semi-infinite space, with the highest positive instantaneous force peaks for the bubbly charge and the continuous water charge being observed at ~3 and 0.5 ms, respectively, i.e., at moments when the shock wave emerges from the right opening of the water duct, being accompanied by the ejection of a portion of medium through this opening. Further, in the second stage, until the time 15–16 ms, a slow increase of instantaneous force is observed in both cases, caused by the progressive acceleration of the medium by the gas bubble expanding from the shock wave generator. The subsequent reduction of the force F (third stage) is associated with the decrease of gas pressure in the duct due to the escape of the gas bubble through the right end of the duct and, also, due to the ejection of fluid through the left end thereof. In general, Fig. 8 shows that, in both cases, the instantaneous force F acting on the device is almost always positive for 50–60 ms after the opening of the diaphragm, decreasing later to zero (fourth stage). As might be expected, the areas under the curve in Fig. 8a, determining the work done by the expanding gas, turned out to be identical to within 2–3%.

The shape of the curves in the initial stages of the process (Fig. 8b) shows that, the use of bubbly water charge in the duct makes it possible to produce a higher instantaneous force than in the case of a continuous water charge. In the first case, the peak instantaneous force acting on the device reaches 100 kN/m, whereas in the second case, the peak instantaneous force does not exceed 70 kN/m. Furthermore, in the first case, the peak is longer: 1 ms instead of 0.2 ms. In more detail, this effect is illustrated in Fig. 9, showing how the average force acting on the device varies with

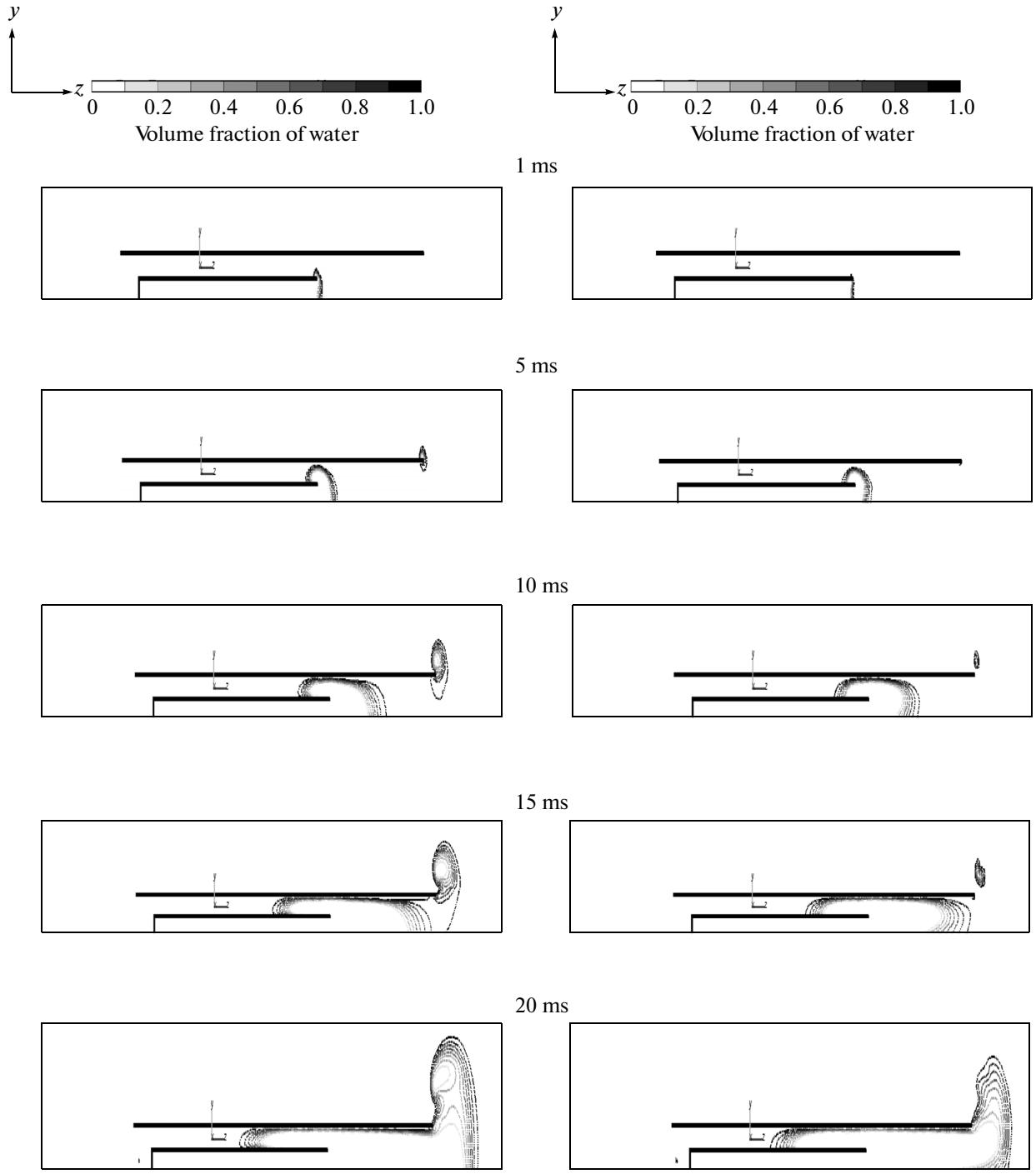

Fig. 7. Calculated isolines of the volume fraction of water α_2 at different points in time after the opening of the diaphragm in the shock wave generator (plotted at a step of 0.1). Panels on the left refer to a bubbly water charge with $\alpha_{20} = 0.9$; those on the right, to a continuous water charge, $\alpha_{20} = 1$.

time t at $\alpha_{20} = 1$, 0.97, 0.94, 0.9, and 0.8 (the first series of calculations). The average force is defined as

$$\bar{F}(t) = \frac{1}{t}\int_0^t F(t)dt.$$

Figure 9 shows that the increase of the initial volume fraction of gas in the bubble charge leads, on the one hand, to the growth of the peak value of the positive average force as compared to that in the continuous water charge (dashed curve), while on the other, to an increase in the duration of the peak level of the neg-

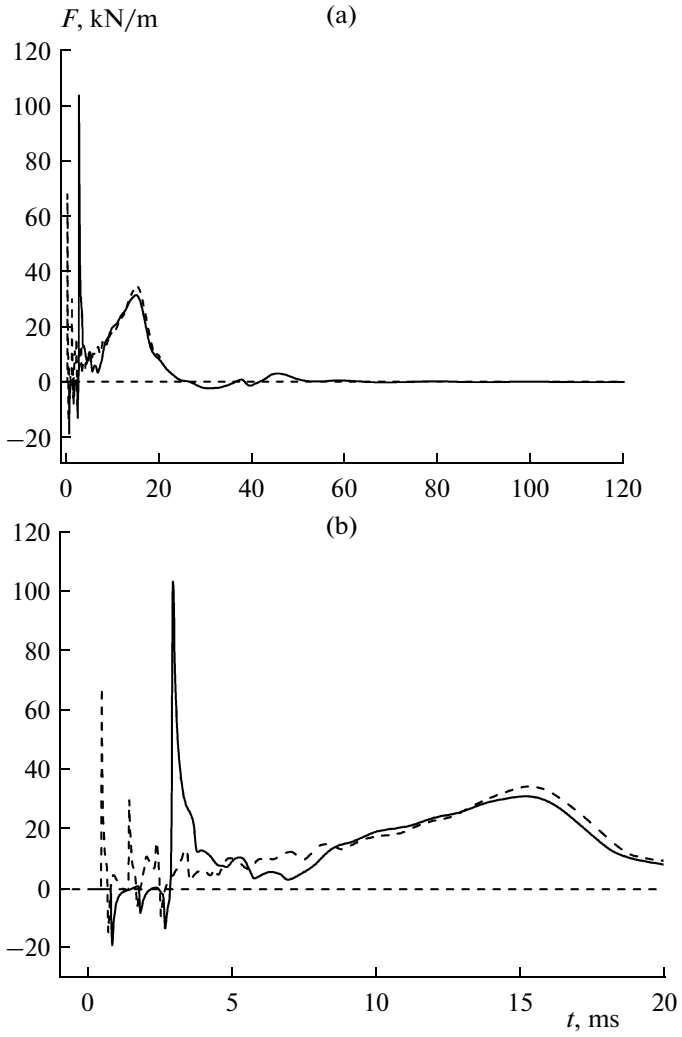

Fig. 8. Calculated time evolution of the instantaneous force acting on the device during momentum transfer from a shock wave to a bubbly water charge with $\alpha_{20} = 0.9$ (solid line) and to a continuous water charge with $\alpha_{20} = 1$ (dashed line): (a) flow duration is 120 ms, (b) initial 20-ms portion of (a).

ative average force at the beginning of the process. Note that the $\bar{F}(t)$ dependence for the continuous water charge features no portions with negative average force. After 12–14 ms, the average force $\bar{F}(t)$ becomes independent of the initial gas content of the water charge in the duct.

Negative values of the mean force for bubbly water charges occur because the velocities of the pressure waves that begin to propagate in a bubbly and a continuous liquid after the arrival of the shock wave from the gas at its boundary with the bubbly liquid differ substantially from each other: the pressure wave in the bubbly liquid propagates much more slowly than it does in the continuous liquid. Therefore, the pressure wave traveling to the left through a continuous liquid in the duct causes an earlier ejection of the liquid through the left end of the duct than through the right end. This conclusion is confirmed by the data in Fig. 10, which shows the average force exerted on the device as a function of time t for three variants of filling of the duct with bubbly liquid at $\alpha_{20} = 0.9$ (second series of calculations). Curves *1–3* correspond, respectively, to the variants in which only region I, regions I and II, and I, II, and III are filled (Fig. 6). It is clear that additional filling of the duct with bubbly liquid (curves *2* and *3* in Fig. 10) enables to eliminate the initial portion with negative average force, thereby making the average force greater than the corresponding value for a continuous water charge (Fig. 9) at times up to 6–7 ms.

CONCLUSIONS

Thus, based on a system of equations of two-phase compressible viscous flow, a two-dimensional numerical simulation of momentum transfer by a shock wave propagating from a gas medium to a continuous or bubbly aqueous medium was performed. When a

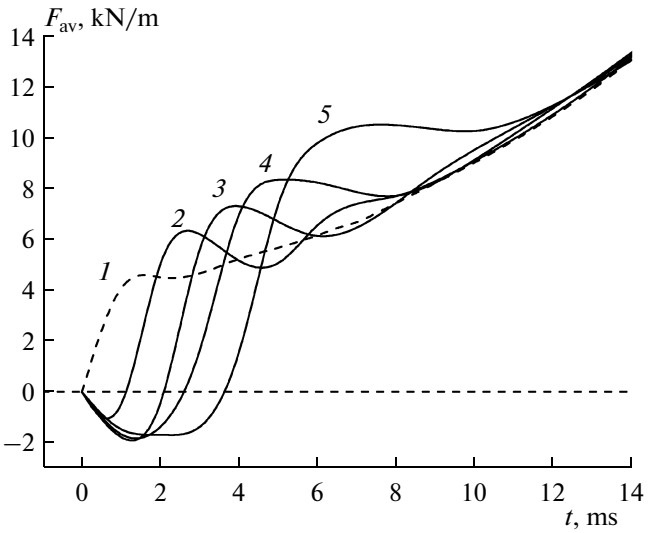

Fig. 9. Calculated time histories of the average force exerted on the device during momentum transfer from a shock wave to (*1*) a continuous water charge ($\alpha_{20} = 1$) and to bubbly water charges with α_{20} = (*2*) 0.97, (*3*) 0.94, (*4*) 0.9, and (*5*) 0.8.

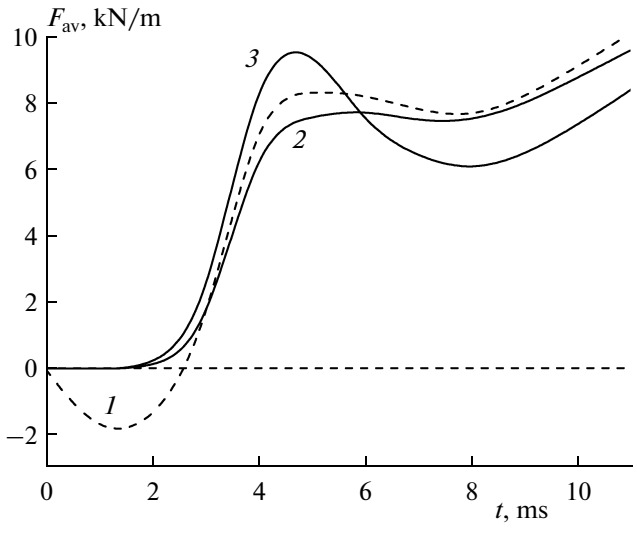

Fig. 10. Calculated time histories of the average force acting on the device for three variants of filling of the water duct with bubbly liquid with $\alpha_{20} = 0.9$: (*1*) only region I (Fig. 6) is filled; (*2*) regions I and II, and (*3*) regions I, II, and III.

shock wave impinges on a continuous incompressible aqueous medium, the latter is set in motion by the gas overpressure after the reflection of shock wave from the gas–liquid interface. By contrast, when a shock wave impinges on a bubbly aqueous medium, the latter is set in motion by the shock wave penetrated into it. Parametric calculations have shown that the momentum transfer from a shock wave to a bubbly liquid can be accompanied by dynamic effects, which ensure that, for some time, the momentum transferred to the bubbly liquid can greatly exceed the momentum transferred to the continuous liquid, all other things being equal. These dynamic effects can be used to create energy-efficient hydrojet propulsion units.

ACKNOWLEDGMENTS

This work was supported by the Ministry of Education and Science of the Russian Federation under the state contract no. 14.609.21.0001 (contract ID RFMEFI57914X0038) "Development of Technology for Creating Hydrojet Thrust in Water-Jet Engines of High-Speed Water Vehicles and the Construction of a Demonstration Prototype of a Hydrojet Pulse-Detonation Engine" within the framework of the federal target program "Research and Development on Priority Directions of Scientific-Technological Complex of Russia in 2014–2020."

APPENDIX

Consider the isothermal two-phase flow of a viscous liquid–gas medium, described by Eq. (1) with constant initial conditions for all the variables:

$$W(x, y, z, 0) = W_0, \tag{A.1}$$

where W is the vector of dependent variables. Then, at $t > 0$, we obtain a constant solution in all the variables.

To investigate whether the evolution problem is well-posed, it is necessary to check whether the solution continuously depends on the initial conditions. Let us perturb initial conditions (A.1) as

$$W'(0, x, y, z) = W_0 + W^{\delta}\sin(ax)\sin(by)\sin(cz), \tag{A.2}$$

where a, b, and c are the perturbation frequencies, not all simultaneously zeros, and W^{δ} is the perturbation amplitude.

Let us now linearize system (1) in the vicinity of the constant solution W_0:

$$W(t, x, y, z) = W_0 + W'(t, x, y, z). \tag{A.3}$$

Substituting (A.3) into (1), assuming that the perturbations of all parameters are small, and neglecting the second-order small terms reduces the system to a canonical form. As a result, we obtain a linear system of equations with constant coefficients:

$$E\frac{\partial W'}{\partial t} + A\frac{\partial W'}{\partial x} + B\frac{\partial W'}{\partial y} + C\frac{\partial W'}{\partial z} + D\frac{\partial^2 W'}{\partial x^2} + F\frac{\partial^2 W'}{\partial y^2} + G\frac{\partial^2 W'}{\partial z^2} + H\frac{\partial^2 W'}{\partial x \partial y} + J\frac{\partial^2 W'}{\partial x \partial z} + K\frac{\partial^2 W'}{\partial y \partial z} = 0. \tag{A.4}$$

The solution to Eq. (A.4) will be sought in the form

$$W'(t, x, y, z) = W^{\delta} e^{i(\omega t + ax + by + cz)}. \tag{A.5}$$

Substituting (A.5) into (A.4) and dividing both sides by $R^2 = a^2 + b^2 + c^2$, yields

$$\left[M(a,b,c) + \frac{i\omega}{R^2} E \right] W^{\delta} = 0, \quad \text{(A.6)}$$

where

$$M(a,b,c) = \frac{1}{R^2}\Big(Aia + Bib + Cic - Da^2 - Fb^2 - Gc^2 - Hab - Jac - Kbc \Big).$$

For system (A.6) to have a nontrivial solution, its determinant must be zero:

$$\left\| M(a,b,c) + \frac{i\omega}{R^2} E \right\| = 0. \quad \text{(A.7)}$$

The solution to the characteristic equation (A.7) is the function $\omega(a,b,c)$. The Cauchy problem for system (1) with initial conditions (A.1) is correct if there is a constant $\bar{C}$, such that, for all $a, b, c \in \mathcal{R}$, the inequality $\mathrm{Im}[\omega(a,b,c)] \geq -\bar{C}$ holds. The issue whether such a problem is well-posed is usually associated with high-frequency perturbations $R^2 = (a^2 + b^2 + c^2) \to \infty$, since ω is limited at any finite R.

Let us introduce the notations

$$\lambda = -\frac{\omega i}{R^2}, \quad a = R\sin(\theta)\cos(\chi), \quad b = R\sin(\theta)\sin(\chi), \quad c = R\cos(\theta) \quad \text{(A.8)}$$

and recast (A.7) in terms of the variables (R, θ, χ). In this case, λ is the eigenvalue of the matrix $M(1/R, \theta, \chi)$. To check whether the values

$$\omega\left(\frac{1}{R}, \theta, \chi\right) = -i\lambda\left(\frac{1}{R}, \theta, \chi\right) R^2$$

are limited, we expanded $R \to \pm\infty$ in the small parameter $\varepsilon = 1/R$: $\lambda = \lambda_0 + \lambda_1\varepsilon + \lambda_2\varepsilon^2 + o(\varepsilon^3)$, where λ_0 is the eigenvalue of the matrix $M_0 = M(0, \theta, \chi)$. Now, the well-posedness condition can be formulated differently: the Cauchy problem for system (1) with initial conditions (A.1) is well-posed if all the eigenvalues of the matrix M satisfy one of the conditions

$$\mathrm{Re}[\lambda_0] > 0,$$

$$\mathrm{Re}[\lambda_0] = 0 \quad \text{and} \quad \mathrm{Re}[\lambda_1] = 0.$$

In this case, the left-hand side of Eq. (A.7) is a polynomial of degree eight. The matrix M_0 yields six positive real values:

$$\lambda_0^{(1,2)} = \frac{\mu_1}{\rho_1}, \lambda_0^{(3)} = \frac{4\mu_1}{3\rho_1}, \lambda_0^{(4,5)} = \frac{\mu_2}{\rho_2}, \lambda_0^{(6)} = \frac{4\mu_2}{3\rho_2},$$

which satisfy the condition of well-posedness, and the double root $\lambda_0^{(7,8)} = 0$, for which, it is necessary to examine the next term of the expansion $\lambda_1^{(7,8)}$. The eigenvalue is a non-differentiable function of the parameter ε at the point $\varepsilon_0 = 0$.

Let us perturb the parameter ε in a vicinity of ε_0 and use the theorem on the bifurcation of a semisimple double eigenvalue [17]. In our case, as a result of bifurcation, the eigenvalue λ splits in the vicinity of $\varepsilon_0 = 0$ into two eigenvalues:

$$\lambda^{(7)} = i\left[w_1\cos\theta + \sin\theta(u_1\cos\chi + v_1\sin\chi)\right]\varepsilon + o(\varepsilon^2),$$

$$\lambda^{(8)} = i\left[w_2\cos\theta + \sin\theta(u_2\cos\chi + v_2\sin\chi)\right]\varepsilon + o(\varepsilon^2),$$

where u, v, and w are the velocity components of the gas (subscript 1) and liquid (index 2). Thus, $\mathrm{Re}[\lambda_1^{(7,8)}] = 0$ and, hence, the Cauchy problem for system (1) with initial conditions (A.1) is well-posed.

REFERENCES

1. S. V. Kulikov and M. F. Khramkin, *Water Jets (Theory and Calculation*) (Sudostroenie, Leningrad, 1980) [in Russian].
2. N. B. Slizhevskii, Yu. M. Korol', and M. G. Sokolik, *Calculation of Propulsion Speed Vessels and Dynamically Supported Ones*, Ed. by N. B. Slizhevskii (NUK, Nikolaev, 2006) [in Russian].
3. Ya. B. Zeldovich, Zh. Eksp. Teor. Fiz. **10**, 543 (1940).
4. S. M. Frolov, *Pulse Detonation Engines*, Ed. by S. M. Frolov (Torus Press, Moscow, 2006) [in Russian].
5. S. S. Kutateladze and V. E. Nakoryakov, *Waves and Heat and Mass Transfer in Liquid–Gas Systems* (Nauka, Novosibirsk, 1984) [in Russian].
6. S. M. Frolov, F. S. Frolov, V. S. Aksenov, and K. A. Avdeev, Invention Application No. PCT/RU2013/001148 (2013). http://idgcenter.ru/patentPCT-RU2013-001148.htm
7. R. I. Nigmatulin, *Dynamics of Multiphase Media* (Nauka, Moscow, 1987; Hemisphere, Washington, 1991), Pt. 1.
8. B. V. Lidskii, V. S. Posvyanskii, I. V. Semenov, R. R. Tukhvatulina, and S. M. Frolov, in *Combustion and Explosion*, Ed. by S. M. Frolov (Torus Press, Moscow, 2013), Vol. 6, p. 137 [in Russian].
9. J. H. Stukmiller, Int. J. Multiphase Flow **3**, 551 (1977).
10. R. Saurel and O. Lemetayer, J. Fluid Mech. **431**, 239 (2001).
11. Yu. B. Radvogin, V. S. Posvyanskii, and S. M. Frolov, J. Phys. IV France, No. 12, 437 (2002).
12. S. Patankar, *Numerical Heat Transfer and Fluid Flow*, Hemisphere Series on Computational Methods in Mechanics and Thermal Science (Hemisphere, Washington, D.C., 1980; Energoatomizdat, Moscow, 1984).
13. M. Yasuo, H. Kunia, and K. Atsutomo, Int. J. Multiphase Flow **2**, 139 (1975).
14. A. I. Sychev, Tech. Phys. **55**, 783 (2010).
15. V. E. Nakoryakov, B. G. Pokusaev, I. R. Shreiber, V. V. Kuznetsov, and N. V. Malykh, *Wave Processes in Two-Phase Systems*, Ed. by S. S. Kutateladze (Inst. Teplofiz. SO AN SSSR, Novosibirsk, 1975), p. 54 [in Russian].
16. S. P. Kalra and Y. Zvirin, Int. J. Multiphase Flow **7**, 115 (1981).
17. A. A. Mailybaev and A. P. Seyranian, *Multiparameter Stability Theory with Mechanical Applications* (Fizmatlit, Moscow, 2009; World Scientific, New Jersey, 2003).

Translated by V. Smirnov